Research Article Vol. 31, No. 2 / 16 Jan 2023 / Optics Express 2768
Optics EXPRESS

Stratospheric aerosol lidar with a 300 µm diameter superconducting nanowire single-photon detector at 1064 nm

MANYI LI,[1] YUNBIN WU,[1] JINLONG YUAN,[1,2] LIJIE ZHAO,[1] DAWEI TANG,[1] JINGJING DONG,[2,3] HAIYUN XIA,[1,2,3,4,5,*] AND XIANKANG DOU[1,5]

[1]*School of Earth and Space Science, University of Science and Technology of China, Hefei 230026, China*
[2]*Collaborative Innovation Center on Forecast and Evaluation of Meteorological Disasters, Nanjing University of Information Science and Technology, Nanjing 210044, China*
[3]*Aerosol-Cloud-Precipitation Key Laboratory, Nanjing University of Information Science and Technology, CMA, Beijing 100081, China*
[4]*Institute of Software, Chinese Academy of Sciences, Beijing 100190, China*
[5]*Hefei National Laboratory for Physical Sciences at Microscale and Department of Modern Physics, University of Science and Technology of China, Hefei, Anhui 230026, China*
[*]*hsia@ustc.edu.cn*

Abstract: Stratospheric aerosols play an important role in the atmospheric chemical and radiative balance. To detect the stratospheric aerosol layer, a 1064 nm lidar with high resolution and large dynamic range is developed using a superconducting nanowire single-photon detector (SNSPD). Measurements are typically performed at 1064 nm for its sensitivity to aerosol, whereas detectors are limited by low efficiency and high dark count rate (DCR). SNSPDs are characterized by high efficiency in the infrared wavelength domain, as well as low noise and dead time, which can significantly enhance the signal quality. However, it is still challenging to build an SNSPD with both large active area and high count rate. To improve the maximal count rate (MCR) so as to avoid saturation in the near range, a 16-pixel interleaved SNSPD array and a multichannel data acquisition system are developed. As a reference, a synchronous system working at 532 nm is applied. In a continuous comparison experiment, backscatter ratio profiles are retrieved with resolutions of 90 m/3 min, and the 1064 nm system shows better performance, which is sensitive to aerosols and immune to the contamination of the ozone absorption and density of molecule change in the lower stratosphere.

1. Introduction

Interests in stratospheric aerosol have increased over the last several decades, for its prominent role in atmospheric climate and chemistry. Quantitative observations of stratospheric aerosol were first achieved by balloon-borne impactors, providing vertical profiles of the particle size distribution and compositions [1]. Since the 1970s, balloon-borne particle counters and condensation nuclei counters were employed routinely to record vertical profiles of size-resolved aerosol concentrations [2–4]. Long-term records indicate that major volcanic events are the dominant factor of stratospheric aerosol abundance variations [2], which may cause subtle surface temperature changes [5], more profound surface cooling [6,7], and related precipitation changes [8–11].

Sporadic but powerful volcanic eruptions injected sulfur into the lower stratosphere [12]. In 1991, the eruption in Mt Pinatubo injected plentiful particulate matter and gaseous SO_2 into the stratosphere, which turned out to be a variety of compounds, including carbonyl sulfide (OCS), sulfuric acid (H_2SO_4), and sulfuric acid/water (H_2SO_4-H_2O) solution droplets [13]. The eruption

#475124 https://doi.org/10.1364/OE.475124
Journal © 2023 Received 7 Sep 2022; revised 19 Nov 2022; accepted 20 Nov 2022; published 11 Jan 2023

Optics EXPRESS

increased the stratospheric sulfur burden to 60 times above nonvolcanic levels, resulting in a transient negative forcing that exceeded greenhouse-gas forcing between mid-1991 and the end of 1992 [14]. The devastating volcanic eruption raised an urgent need for stratospheric aerosol detection, for its importance in understanding the transport, residence, and dissipation processes, as well as predicting subsequent impacts.

Nowadays, lidar remote sensing is regarded as a promising and significant tool due to its superiorities of high spatial/temporal resolution, high accuracy, and the ability to cover the altitude range from the boundary layer to the mesosphere. Early stratospheric aerosol lidar measurements began in 1969, using a ruby laser at 694.3 nm and a twilight gradient approach [15]. An elastic backscatter lidar with single-photon counting and analog detection has been used to detect stratospheric aerosol since 1976 [16]. In our previous work, stratospheric aerosol was also found in atmospheric density and temperature measurements [17–19]. In the Rayleigh integration lidar detection, the retrieval of density and temperature relies on the assumption of no aerosol. When the total lidar backscatter is contaminated by aerosol, the measurement results are perturbed. For the past several years, stratospheric aerosol lidars are increasingly applied in observing the plume of volcanic eruptions [20–22].

To retrieve optical properties of aerosols from backscatter lidar, the signal must be precisely calibrated. A common and preferred method is the Rayleigh normalization technique, which calibrates the Rayleigh component of the backscatter signal from attitude ranges without aerosol [23]. James D. Klett and Frederick G. Fernald proposed an approach to solving the single-scattering lidar equation with the extinction-backscattering ratio [24,25]. Two methods that can be applied to retrieve aerosol extinction coefficients are Raman backscatter lidar technique [26,27] and the high spectral resolution lidar (HSRL) technique [28–30], based on spectrally filtering the narrow-band aerosol component. Both techniques have been widely applied in tropospheric lidars rather than stratospheric aerosol lidars [12].

For better response to the aerosol component, the infrared wavelength domain is commonly regarded as an advantageous band for its sensitivity to aerosol particles. Restricted by the energy of a fiber laser, 1.5 μm lidar is better suited for low altitude aerosol detection [31–33], whereas 1.0 μm lidar can use a high-energy solid-state laser for tropospheric and stratospheric detection [34]. However, detectors at 1.0 μm, such as Si-based or InGaAs/InP-based avalanche photodiodes (APD), are typically limited by low efficiency, low maximal count rate (MCR), high dark count rate (DCR), and after-pulsing [35]. Fortunately, due to appealing characteristics of wide spectral range, high quantum efficiency, low DCR, and low timing jitter [36–38], superconducting nanowire single-photon detector (SNSPD) is an effective solution that attracts an increasing number of sights. SNSPD has demonstrated eminent performance in laser ranging [39–41], quantum communications [42], and atmospheric remote sensing [43–45].

However, these SNSPDs are generally single-mode fiber (SMF) coupled, resulting in non-qualification for long-range detection. Multi-mode fibers (MMF) can provide larger numerical apertures (NAs) and core diameters, thus reducing the disturbances of coupling efficiency between telescope and fiber. Circular NbN based single-pixel SNSPD with the diameter of 100 μm was realized, resulting in a detection efficiency of 65% at 532 nm [46]. Nonetheless, it is challenging of SNSPD with both an ultra-large-active area and high count rate, because MCR is squared inversely proportional to the diameter of active area [47]. To solve this problem, the design of multi-pixel array has been adopted to extend the active area [48], thereby increasing the total MCR of SNSPD. 9-pixel SNSPD has been fabricated working at the wavelength of 1064 nm, and its MCR exceeds 43 MHz when coupled with 200 μm diameter MMF [49]. Recently, a 16-pixel SNSPD system coupled with 62.5 μm diameter MMF was applied in atmosphere helium resonance lidar detection at the wavelength of 1083 nm [50].

In this work, a Rayleigh-Mie lidar incorporating a 16-pixel interleaved SNSPD array and photomultiplier tube (PMT) is proposed and experimentally demonstrated. For the first time,

Optics EXPRESS

a 1064 nm NbN SNSPD with a 300 μm diameter active area and total MCR of 50 MHz is employed in stratospheric aerosol detection. Meanwhile, a matched readout circuit is designed and fabricated to avoid count loss during the acquisition process. The calibrated count rate of the incident photons exceeds 300 MHz., and backscatter signal of the desired signal-to-noise ratio (SNR) from 10 to 80 km is recorded. In the experiment section, the stratospheric aerosol layer at altitude about 25 km is observed, proving the ability to identify stratospheric aerosol quantitatively.

2. Instrument

The Rayleigh-Mie lidar system is composed of a pulsed, frequency-stable laser transmitter, a reflecting telescope of dual-wavelength, and a dual-channel receiver including detectors and a data acquisition system. The schematic of the lidar is depicted in Fig. 1. The laser transmitter of the system is based on a Q-switched, flash pumped, and frequency-doubled Nd: YAG laser (Spitlight 2000-50), generating pulses of 50 Hz at 532 and 1064 nm wavelengths. By the injection of a narrow bandwidth fiber laser, the laser works at a stable single longitudinal mode. Main parameters of the Rayleigh-Mie lidar system are listed in Table 1.

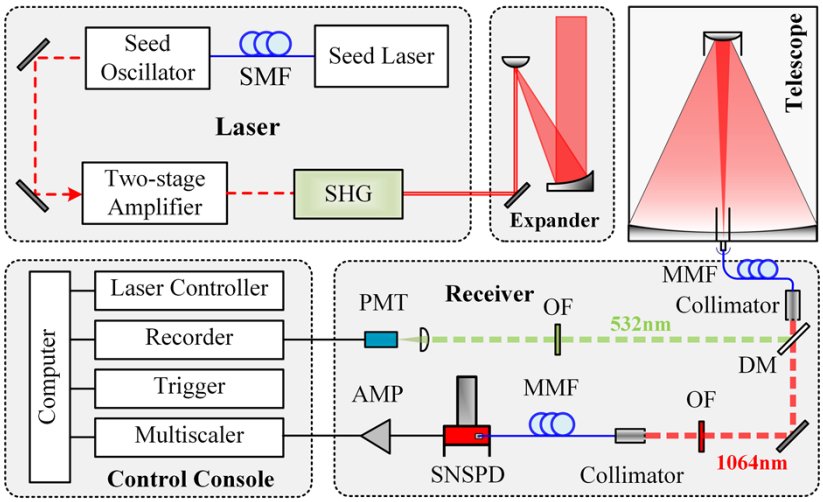

Fig. 1. Schematic diagram of the lidar system. SHG, Second-harmonic Generator; SMF, Single-mode Fiber; MMF, Multi-mode Fiber; DM, Dichroic Mirror; OF, Optical Filter; PMT, Photomultiplier Tube; SNSPD, Superconducting Nanowire Single-photon Detector; AMP, Amplifier.

To prevent potential lens damage caused by dust, reflectors of high damage threshold are employed, and a reflecting beam expander is introduced to compress the divergence of outgoing light. The backscatter signal is collected by a 1-m diameter reflecting telescope with high reflectivity at 532 and 1064 nm, which is designed to increase SNR and reduce the influence of atmospheric turbulence. The photons are then coupled into a multimode fiber with core diameter of 1.5 mm and NA of 0.39, transferring the signals from the telescope to the optical receiver. Then the light is split and collimated into two channels: Photons at 532 nm are detected by a PMT (Hamamatsu H7421-40), and are then recorded by a photon counter board. As shown in Fig. 2(a), photons at 1064 nm are coupled into a 7-nm-thick NbN nanowire, whose width and pitch are 100 and 360 nm, respectively. The NbN thin film was deposited on a Si substrate by magnetron sputtering, and then patterned into the 16-pixel array. The superconducting critical temperatures are around 7.41 K, and the highest bias currents of sustaining superconductivity

Optics EXPRESS

Table 1. Key parameters of the Rayleigh-Mie lidar system

Parameter		1064 nm system	532 nm system
Transmitter			
	Pulse energy (mJ)	1000	30
	Repetition rate (Hz)	50	50
	Divergence (mrad)	0.15	0.15
Receiver			
	Telescope diameter (mm)	1000	1000
	Focal length (mm)	1600	1600
	Fiber core diameter (μm)	300	1500
	Fiber NA	0.39	0.37
	Detector type	SNSPD	PMT
	Active area diameter (μm)	300	5000
	Detection efficiency(%)	31@1064 nm	40@532 nm
	DCR (cps)	500	100
	MCR (MHz)	50	10

are in range of 14.4-15.9 μA [49]. Normally, the nanowire inside a helium dewar operates in a superconducting state at a temperature of 2.2 K. When an incoming photon hits the nanowire, the superconducting state will be broken, and then a voltage signal will be sent to the readout circuit system, as described below. After this event, the nanowire regains superconductivity.

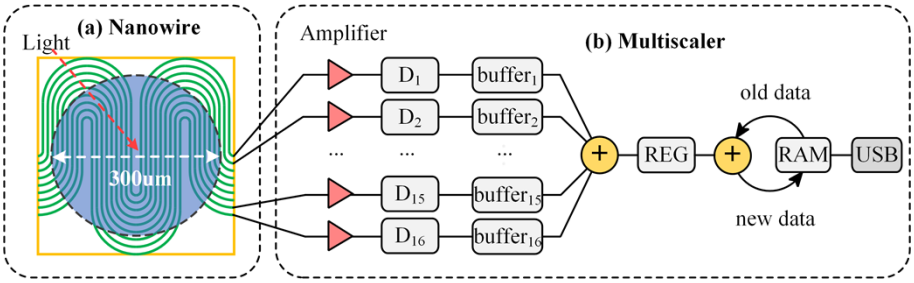

Fig. 2. (a) 16-interleaved nanowire SNSPD array (active area of 300 μm in diameter as denoted by the black dashed circle). (b) Schematic diagram of the multiscaler system. D_i, Discriminator of channel i; REG, Register; RAM, Random Access Memory; USB, Universal Serial Bus.

To match the 16-pixel interleaved SNSPD array, a 16-channel readout circuit system is developed. The detection schematic diagram is shown in Fig. 2(b). First, the electrical signal caused by an incident of single-photon in each pixel is amplified, discriminated, and reshaped as a 3.3 V transistor-transistor logic (TTL) 10 ns pulse. The discriminator's output signals are then sent to a field-programmable gate array (FPGA) to be reshaped as 20 ns width pulses, synchronized with the clock of FPGA. Because the dead time of each probe is greater than 20 ns, the process will not result in count loss. The FPGA samples 16 channels of detection signals simultaneously with a 50 MHz clock, and the sampling results are added and stored in a 32-bit unsigned integer register. Simultaneously, the FPGA reads the accumulated photon counts with the same time stamp from random access memory (RAM) and writes them back into RAM after adding the accumulated count. Following the acquisition process, data stored in RAM records the distribution of photon counts with different time stamps, which are then transferred

Optics EXPRESS

to a computer via USB for further data processing. The acquisition system greatly improves the system's saturation counts rate in the presence of limited RAM reading and writing speed by processing the detection signals with the same time information in different channels on the same rising edge of the clock.

3. Experiment

Three steps of the experiment are presented in this section. First, the lidar raw data from SNSPD and PMT are calibrated. Second, we compare the aerosol retrieval using 532 nm lidar data, 1064 nm lidar data, and both of them. Finally, continuous observation of the stratospheric aerosol layer is conducted with the Rayleigh-Mie lidar working vertically together.

3.1. Receiver calibration

We apply different receiver calibration formulas for PMT and SNSPD. The lidar raw data are processed in the following steps:

-*Dead time correction*. In a detector system, there is a certain amount of time to discriminate between two photon incident events. If N_0 represents count rate calculated from raw data and τ represents dead time, then the corrected count rate N can be written as [51]

$$N = \frac{N_0}{1 - \tau \cdot N_0}. \tag{1}$$

-*Saturation count rate correction*. Many single-photon detectors (for example, single-photon APD, PMT, SNSPD) can only distinguish between zero and more than zero photons [35]. Deviations from the ideal detection impact experiments negatively, thus correction to the detector's response is necessary.

A preliminary experiment is performed to calibrate the SNSPD efficiency at high count rates. Certain intensity of light incidents into 16-pixel interleaved SNSPD array and photon counts are recorded by the data acquisition system. As the incident photon rate increases, the quantum efficiency decreases, as shown in Fig. 3(a). Nonlinearity appears when the input photon rate approaches 40 MHz. The resulting curve is applied to correct the saturating count in the near range of lidar measurements, as shown in Fig. 3(b).

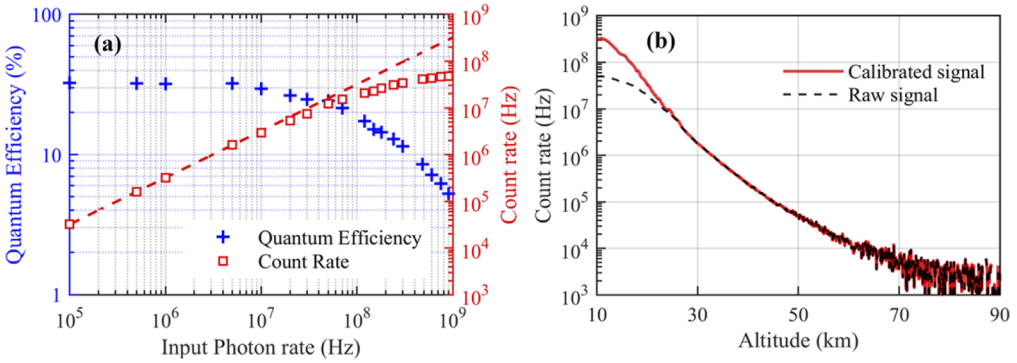

Fig. 3. (a) describes how SNSPD quantum efficiency and count rate change with the input photon rate. The red dashed line shows linearity. (b) lidar signal before and after calibration.

-*Background subtraction*. Mean signal above 100 km is subtracted since backscatter from these altitudes is negligible compared to solar or star background.

Optics EXPRESS

3.2. Comparison of aerosol retrieval

A standard and quantitative parameter to characterize the aerosol content in the atmosphere is the backscatter ratio, R, defined by the following equation:

$$R(\lambda, z) = \frac{\beta_m(\lambda, z) + \beta_a(\lambda, z)}{\beta_m(\lambda, z)}, \tag{2}$$

where the subscripts a and m stand for aerosol and atmospheric molecule, respectively, and $\beta(\lambda, z)$ is the backscatter coefficient of wavelength λ at range z. Using the Klett-Fernald (KF) method [24,25], the aerosol extinction coefficient and backscatter coefficient can be obtained when the extinction-backscattering ratio of aerosol is assumed. The ratio depends on the laser wavelength and various properties of aerosol, generally, the value of sulfate aerosol can be assumed as 30 for the stratosphere and 46 for the troposphere [52]. An initial value of R at a reference altitude z_{ref}, typically in range of 30-40 km where atmosphere is relatively pure and SNR is high enough, is necessary for iteration:

$$\beta_a(\lambda, z_{ref}) = [R(\lambda, z_{ref}) - 1]\beta_m(\lambda, z_{ref}). \tag{3}$$

$R(\lambda, z_{ref})$ can be assumed to be approximately 1.02-1.05 according to experiential value [23,53]. The atmospheric molecule backscatter coefficient can be calculated by the US Standard Atmosphere model and be regarded as stable:

$$\beta_m(\lambda, z) = \frac{P(z)}{k_B T(z)}(5.45 \times 10^{-32})(\frac{\lambda}{550})^{-4.09}, \tag{4}$$

where $P(z)$ is the atmospheric pressure (P_a), $T(z)$ is the temperature (K), and k_B is the Boltzmann constant ($m^2 kgs^{-2}K^{-1}$). With the lidar ratio remaining constant over the range being investigated, the aerosol backscatter ratio can be calculated from the backscatter signal.

In this section, a retrieval method is introduced to make use of the dual-wavelength lidar data, which is called the dual-wavelength method here to make it clearer for definition and comparison. As described below, we normalize the 532 and l064 nm lidar data, and then separate the components of aerosol and molecule using their different color ratios. In contrast, the KF method solves a single-scattering lidar equation by assuming an initial value and iteration, relying on the knowledge of atmospheric molecule background. The total backscatter coefficient at the altitude z can be calculated with:

$$\frac{\beta(\lambda, z)}{\beta(\lambda, z_{ref})} = \frac{N(\lambda, z)}{N(\lambda, z_{ref})} \cdot Tr(\lambda, z - z_{ref})^2, \tag{5}$$

where N denotes the photon number of backscattering and Tr denotes the transmittance between z and z_{ref} which can be estimated with the US Standard Atmosphere model. Such an estimation leads to limited errors because of the thin atmosphere at high altitudes, and hence, the value of Tr close to unity.

Light interacts with aerosol particles variously, depending on the particle size, shape, internal structure, and complex refractive index, as well as the light wavelength. In general, aerosol extinction is often governed by the following simple analytical equation:

$$\sigma(\lambda) = k\lambda^{-\varepsilon}, \tag{6}$$

where σ denotes the extinction coefficient, ε is called the Angstrom wavelength exponent, and k gives the value of the aerosol extinction coefficient at the wavelength 1000 nm [54]. The color

Optics EXPRESS

ratio of molecule and aerosol can be estimated by

$$\frac{\beta_m(\lambda_1, z)}{\beta_m(\lambda_2, z)} = (\frac{\lambda_1}{\lambda_2})^{-4.09}, \tag{7}$$

$$\frac{\sigma_a(\lambda_1, z)}{\sigma_a(\lambda_2, z)} = (\frac{\lambda_1}{\lambda_2})^{-\varepsilon}. \tag{8}$$

To better estimate the value of Angstrom wavelength exponent of stratospheric aerosol, year-averaged aerosol size distribution is applied. The stratospheric aerosol consists of a significant amount of sulfuric acid/water (H2SO4-H2O) solution droplets in the sub-micron size range [13], so the particles can be assumed to be spherical and Mie theory can be applied. The imaginary part of the refractive index, m, or the absorption index, is set to zero since absorption for stratospheric aerosol is very low for visible and near-infrared radiation [55]. Generally, the particle size distribution can be described by a bimodal lognormal function of the following form:

$$n(r) = \frac{C_1}{\sqrt{2\pi}\ln\delta_1 r}\exp\left[-\frac{(\ln r - \ln R_1)^2}{2\ln^2\delta_1}\right] + \frac{C_2}{\sqrt{2\pi}\ln\delta_2 r}\exp\left[-\frac{(\ln r - \ln R_2)^2}{2\ln^2\delta_2}\right], \tag{9}$$

$n(r)$ is the total number density of particles with radius r. For each mode of the distribution, R_i is the median radius, C_i is the peak value, and δ_i is the distribution width.

Distribution from optical particle counter measurement in 1999 [2–4] is adopted to estimate the Angstrom wavelength exponent of non-volcanic period, as shown in Fig. 4. With the model of size distribution, hypothetical extinction coefficient or backscatter coefficient can be calculated using formulas below:

$$\sigma_\lambda = \int_{r_{\min}}^{r_{\max}} \pi r^2 Q_{ext}[r, \lambda, m] n(r) dr, \tag{10}$$

$$\beta_\lambda = \int_{r_{\min}}^{r_{\max}} \pi r^2 Q_b[r, \lambda, m] n(r) dr. \tag{11}$$

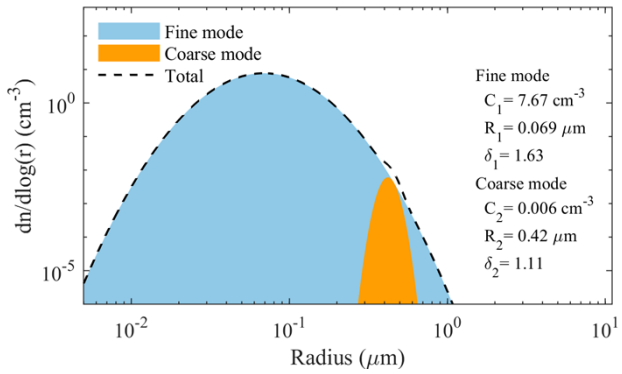

Fig. 4. A typical aerosol size distribution from optical particle counter measurements. Fine and coarse modes are colored in light brown and light coral, and the summary is represented by a black dashed line. Parameters of the bimodal lognormal function are listed in the figure. The distribution was measured at 20 km altitude in 1999 [2–4].

Here, Q_{ext} and Q_b are the extinction efficiency factor and backscatter efficiency factor, respectively, and can be calculated using Mie scattering theory, with a typical complex refractive index value of $m = 1.45 - 0i$, as shown in Fig. 5.

By integrating Eqn. (10) and Eqn. (11) with the radius range from $r_{\min}$ to $r_{\max}$, we can estimate the color ratio of stratospheric aerosol as Eqn. (8).

Optics EXPRESS

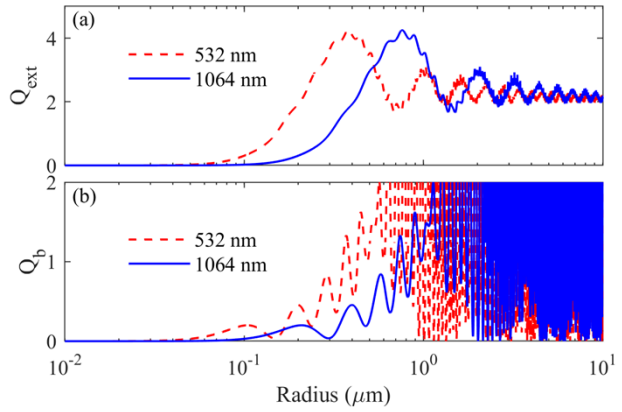

Fig. 5. (a) Extinction efficiency factor Q_{ext} and (b) backscatter efficiency factor Q_b for particles of different radius at wavelength 532 nm (red dashed line) and 1064 nm (blue straight line). Simulation is based on the assumption that complex refractive index is $1.45 - 0i$.

To compare the aerosol retrieval using 532 and 1064 nm lidar data, an experiment was conducted with the dual-wavelength lidar system, as described in the next section. Figure 6 depicts an example of 15 minutes time-averaged lidar data from experiments. Suppose the photon counts obey the Poisson statistics in lidar backscatter, the SNR of the data can be estimated as the square root of signal counts on each detector [56].

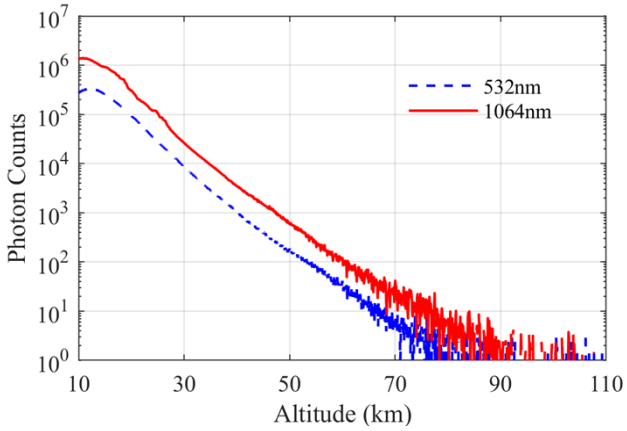

Fig. 6. Time averaged altitude profiles of backscattered signals from 0:00 to 0:15, on Jan. 2 in 2022.

Figure 7 depicts four profiles in the experiment. The backscatter ratio of 532 and 1064 nm are obtained following the KF method, and profiles in blue dashed line are calculated following the dual-wavelength method. Backscatter error of the KF method can be estimated by the previous work [57]. The result shows similar backscatter ratio of 1064 nm between the KF method and the dual-wavelength method, especially above the altitude of 20 km. The backscatter ratio above 27 km tends to be $R = 1$, and an aerosol layer is observed at around 25 km. As shown in Eqn. (4), the atmospheric molecule backscatter coefficient is inversely proportional to the fourth power of the wavelength, in line with the result that backscatter ratio at 532 nm is much smaller than that at 1064 nm. We also note that backscatter ratio of 532 nm lidar signal is smaller than 1 in altitude ranges below 20 km, whereas the backscatter ratio should not be smaller than 1 from the definition

Optics EXPRESS

of Eqn. (2). It could be explained by ozone extinction in transmission, as discussed in a previous study [26]. Meanwhile, the underestimation of the PMT detection saturation may also exert an influence. Inevitably, ozone extinction affects the retrieval of the dual-wavelength method, due to the ozone absorption stronger at 532 nm than at 1064 nm [58]. The result demonstrates the superiority of 1064 nm aerosol lidar for its sensitivity to aerosol and insensitivity to ozone.

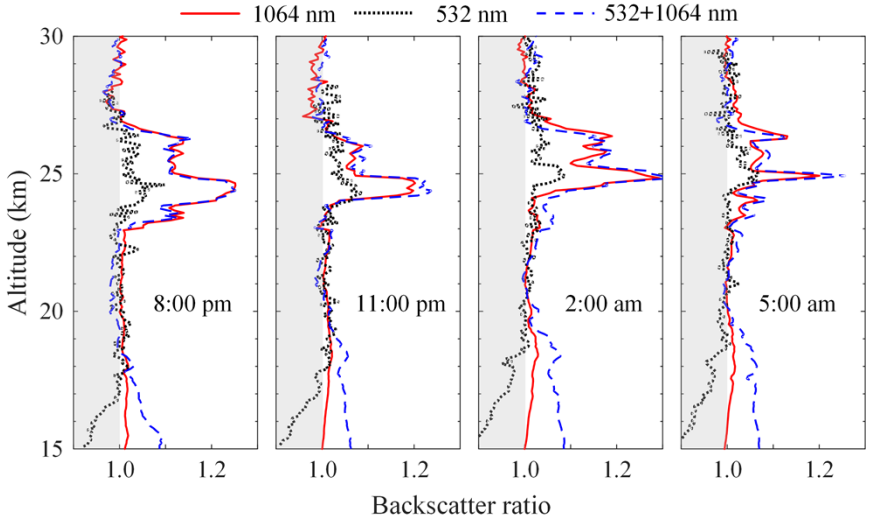

Fig. 7. Comparison of backscatter ratio retrieved from the KF method (red straight line: using 1064 nm lidar data; black dotted line: using 532 nm lidar data) and the dual-wavelength method (blue dashed line). The profiles are depicted from the experiment conducted on Jan.1 to Jan. 2, 2022, and each profile is accumulated in 15 minutes. Local time of each profile is shown in the figure. Value of backscatter ratio below 1 is masked (gray).

3.3. Stratospheric aerosol continuous detection

In order to demonstrate the stability of the system, continuous observation was conducted from 20:00 on Jan. 1 to 6:00 on Jan. 2 in 2022. The measurement was performed on the top of a building at the University of Science and Technology of China (USTC) (31.83°N, 117.25°E). Rayleigh-Mie laser beams are emitted vertically at a height of 50 m above ground.

As mentioned above, the result retrieved from 1064 nm lidar data performs better due to its high response to aerosol and immunity to ozone. Therefore, we calculate the backscatter ratio from 1064 nm lidar data using the KF method, with the lidar ratio of 30 sr along the vertical profile, and an initial value of R = 1.02 at the height of z_{ref}=36 km. Figures 8(a) and (b) show the lidar signal of the 532 and 1064 nm lidar, while the backscatter ratio in Fig. 8(c) based on 1064 nm reveals the evolution of the stratospheric aerosol layer at 25 km during the nighttime. Similarly, stratospheric aerosol layers were found over the Tibetan Plateau in satellite and portable optical particle counter measurements [59]. Figure 8(d) is an enlarged version of Fig. 8(c), and the layer structure and evolution of stratospheric aerosol are recorded clearly (90 m / 3 minutes resolution) and continuously.

Optics EXPRESS

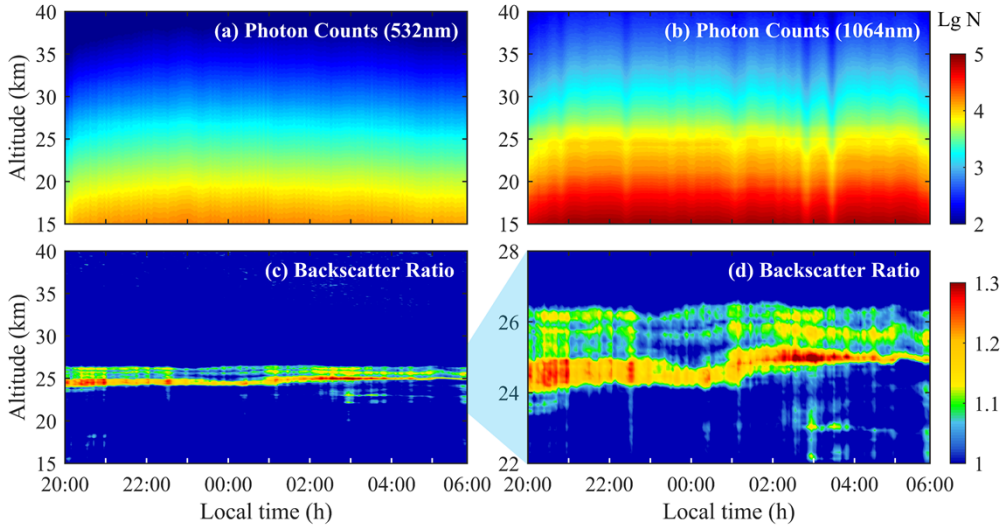

Fig. 8. (a) Backscatter signal of 532 nm lidar; (b) Backscatter signal of 1064 nm lidar; (c) Aerosol backscatter ratio retrieved using 1064 nm lidar data; (d) An enlarged illustration of the aerosol layer around 25 km obtained from (c). The time resolution is 3 minutes and the altitude resolution is 90 m.

4. Conclusion

A 1064 nm lidar base on an SNSPD with a 300-μm diameter active area and high read-out MCR of 50 MHz at 1064 nm is demonstrated. To increase the dynamic detection range, a 16-pixel interleaved SNSPD array and a multichannel readout circuit system are designed and manufactured. By the calibration of the SNSPD response curve, we improve the MCR from 50 to 300 MHz. In contrast, a 532 nm lidar using PMT works synchronously. We compare the backscatter ratio retrieval of 532 nm lidar data, 1064 nm lidar data, and a method using dual-wavelength data. The results indicate that the infrared wavelength performs better in atmospheric aerosol detection due to its sensitivity to aerosol and immunity to ozone. In the future, we plan to observe stratospheric aerosol synchronously with wind and column AOD detection to better retrieve the optical properties and trace the source.

Disclosures. The authors declare that there are no conflicts of interest related to this article.

Data availability. Data underlying the results presented in this paper are not publicly available at this time but may be obtained from the authors upon reasonable request.

References

1. C. E. Junge, C. W. Chagnon, and J. E. Manson, "Stratospheric aerosols," Journal of Atmospheric Sciences **18**, 81–108 (1961).
2. T. Deshler, R. Anderson-Sprecher, H. Jäger, J. Barnes, D. J. Hofmann, B. Clemesha, D. Simonich, M. Osborn, R. G. Grainger, and S. Godin-Beekmann, "Trends in the nonvolcanic component of stratospheric aerosol over the period 1971–2004," J. Geophys. Res. **111**(D1), D01201 (2006).
3. T. Deshler, M. E. Hervig, D. J. Hofmann, J. M. Rosen, and J. B. Liley, "Thirty years of in situ stratospheric aerosol size distribution measurements from Laramie, Wyoming (41°N), using balloon-borne instruments," J. Geophys. Res. **108**(D5), 4167 (2003).
4. D. Hofmann, J. Rosen, T. Pepin, and R. Pinnick, "Stratospheric aerosol measurements. I- Time variations at northern midlatitudes," J. Atmos. Sci. **32**(7), 1446–1456 (1975).
5. S. Solomon, J. S. Daniel, R. R. Neely III, J.-P. Vernier, E. G. Dutton, and L. W. Thomason, "The persistently variable "background" stratospheric aerosol layer and global climate change," Science **333**(6044), 866–870 (2011).
6. J. Hansen, A. Lacis, R. Ruedy, and M. Sato, "Potential climate impact of Mount Pinatubo eruption," Geophys. Res. Lett. **19**(2), 215–218 (1992).
7. A. Robock and J. Mao, "The volcanic signal in surface temperature observations," J. Clim. **8**(5), 1086–1103 (1995).

Optics EXPRESS

8. J. M. Haywood, A. Jones, N. Bellouin, and D. Stephenson, "Asymmetric forcing from stratospheric aerosols impacts Sahelian rainfall," Nat. Clim. Change **3**(7), 660–665 (2013).
9. C. E. Iles, G. C. Hegerl, A. P. Schurer, and X. Zhang, "The effect of volcanic eruptions on global precipitation," J. Geophys. Res. Atmos. **118**(16), 8770–8786 (2013).
10. F. Liu, J. Chai, B. Wang, J. Liu, X. Zhang, and Z. Wang, "Global monsoon precipitation responses to large volcanic eruptions," Sci. Rep. **6**(1), 24331–11 (2016).
11. G. Gu and R. F. Adler, "Precipitation and temperature variations on the interannual time scale: Assessing the impact of ENSO and volcanic eruptions," J. Clim. **24**(9), 2258–2270 (2011).
12. S. Kremser, L. W. Thomason, M. von Hobe, M. Hermann, T. Deshler, C. Timmreck, M. Toohey, A. Stenke, J. P. Schwarz, R. Weigel, S. Fueglistaler, F. J. Prata, J.-P. Vernier, H. Schlager, J. E. Barnes, J.-C. Antuña-Marrero, D. Fairlie, M. Palm, E. Mahieu, J. Notholt, M. Rex, C. Bingen, F. Vanhellemont, A. Bourassa, J. M. C. Plane, D. Klocke, S. A. Carn, L. Clarisse, T. Trickl, R. Neely, A. D. James, L. Rieger, J. C. Wilson, and B. Meland, "Stratospheric aerosol-Observations, processes, and impact on climate," Rev. Geophys. **54**(2), 278–335 (2016).
13. L. W. Thomason and T. Peter, "*Assessment of stratospheric aerosol properties (ASAP)*," (SPARC report, 2006).
14. M. P. McCormick, L. W. Thomason, and C. R. Trepte, "Atmospheric effects of the Mt Pinatubo eruption," Nature **373**(6513), 399–404 (1995).
15. K. Bartusek and D. Gambling, "Simultaneous measurements of stratospheric aerosols using lidar and the twilight technique," J. Atmos. Terr. Phys. **33**(9), 1415–1430 (1971).
16. T. Trickl, H. Giehl, H. Jäger, and H. Vogelmann, "35 yr of stratospheric aerosol measurements at Garmisch-Partenkirchen: from Fuego to Eyjafjallajökull, and beyond," Atmos. Chem. Phys. **13**(10), 5205–5225 (2013).
17. H. Xia, X. Dou, M. Shangguan, R. Zhao, D. Sun, C. Wang, J. Qiu, Z. Shu, X. Xue, and Y. Han, "Stratospheric temperature measurement with scanning Fabry-Perot interferometer for wind retrieval from mobile Rayleigh Doppler lidar," Opt. Express **22**(18), 21775–21789 (2014).
18. J. Ma, M. Shangguan, H. Xia, X. Fang, X. Xue, and X. Dou, "Rayleigh and sodium lidar system incorporating time-division and wavelength-division multiplexing," Opt. Commun. **448**, 116–123 (2019).
19. H. Xia, X. Dou, D. Sun, Z. Shu, X. Xue, Y. Han, D. Hu, Y. Han, and T. Cheng, "Mid-altitude wind measurements with mobile Rayleigh Doppler lidar incorporating system-level optical frequency control method," Opt. Express **20**(14), 15286–15300 (2012).
20. G. Vaughan, D. Wareing, and H. Ricketts, "Measurement Report: Lidar measurements of stratospheric aerosol following the 2019 Raikoke and Ulawun volcanic eruptions," Atmos. Chem. Phys. **21**(7), 5597–5604 (2021).
21. L. Bitar, T. Duck, N. Kristiansen, A. Stohl, and S. Beauchamp, "Lidar observations of Kasatochi volcano aerosols in the troposphere and stratosphere," J. Geophys. Res. **115**, D00L13 (2010).
22. A. T. Prata, S. A. Young, S. T. Siems, and M. J. Manton, "Lidar ratios of stratospheric volcanic ash and sulfate aerosols retrieved from CALIOP measurements," Atmos. Chem. Phys. **17**(13), 8599–8618 (2017).
23. R. Collis and P. Russell, "Lidar measurement of particles and gases by elastic backscattering and differential absorption," Laser monitoring of the atmosphere **14**, 71–151 (1976).
24. James D. Klett, "Lidar inversion with variable backscatter/extinction ratios," Appl. Opt. **24**(11), 1638–1643 (1985).
25. F. G. Fernald, "Analysis of atmospheric lidar observations: some comments," Appl. Opt. **23**(5), 652–653 (1984).
26. A. Langenbach, G. Baumgarten, J. Fiedler, F.-J. Lübken, C. von Savigny, and J. Zalach, "Year-round stratospheric aerosol backscatter ratios calculated from lidar measurements above northern Norway," Atmos. Meas. Tech. **12**(7), 4065–4076 (2019).
27. S. Melfi, "Remote measurements of the atmosphere using Raman scattering," Appl. Opt. **11**(7), 1605–1610 (1972).
28. C. She, R. Alvarez, L. Caldwell, and D. Krueger, "High-spectral-resolution Rayleigh–Mie lidar measurement of aerosol and atmospheric profiles," Opt. Lett. **17**(7), 541–543 (1992).
29. J. W. Hair, C. A. Hostetler, A. L. Cook, D. B. Harper, R. A. Ferrare, T. L. Mack, W. Welch, L. R. Izquierdo, and F. E. Hovis, "Airborne high spectral resolution lidar for profiling aerosol optical properties," Appl. Opt. **47**(36), 6734–6752 (2008).
30. D. Xiao, N. Wang, X. Shen, E. Landulfo, T. Zhong, and D. Liu, "Development of ZJU high-spectral-resolution LiDAR for aerosol and cloud: Extinction retrieval," Remote Sens. **12**(18), 3047 (2020).
31. H. Xia, G. Shentu, M. Shangguan, X. Xia, X. Jia, C. Wang, J. Zhang, J. S. Pelc, M. Fejer, and Q. Zhang, "Long-range micro-pulse aerosol lidar at 1.5 μm with an upconversion single-photon detector," Opt. Lett. **40**(7), 1579–1582 (2015).
32. J. Yuan, Y. Wu, Z. Shu, L. Su, D. Tang, Y. Yang, J. Dong, S. Yu, Z. Zhang, and H. Xia, "Real-Time Synchronous 3-D Detection of Air Pollution and Wind Using a Solo Coherent Doppler Wind Lidar," Remote Sens. **14**(12), 2809 (2022).
33. X. Shang, H. Xia, X. Dou, M. Shangguan, M. Li, and C. Wang, "Adaptive inversion algorithm for 1.5 μm visibility lidar incorporating in situ Angstrom wavelength exponent," Opt. Commun. **418**, 129–134 (2018).
34. H. Xia, D. Sun, Y. Yang, F. Shen, J. Dong, and T. Kobayashi, "Fabry-Perot interferometer based Mie Doppler lidar for low tropospheric wind observation," Appl. Opt. **46**(29), 7120–7131 (2007).
35. M. D. Eisaman, J. Fan, A. Migdall, and S. V. Polyakov, "Invited review article: Single-photon sources and detectors," Rev. Sci. Instrum. **82**(7), 071101 (2011).
36. W. Zhang, J. Huang, C. Zhang, L. You, C. Lv, L. Zhang, H. Li, Z. Wang, and X. Xie, "A 16-pixel interleaved superconducting nanowire single-photon detector array with a maximum count rate exceeding 1.5 GHz," IEEE Trans. Appl. Supercond. **29**(8), 1–7 (2019).

Optics EXPRESS

37. Y. Guan, H. Li, L. Xue, R. Yin, L. Zhang, H. Wang, G. Zhu, L. Kang, J. Chen, and P. Wu, "Lidar with superconducting nanowire single-photon detectors: Recent advances and developments," Opt. Lasers Eng. **156**, 107102 (2022).
38. J. C. Bienfang, V. Zwiller, and S. Steinhauer, "Materials, devices, and systems for high-speed single-photon counting," MRS Bull. **47**(5), 494–501 (2022).
39. L. Xue, Z. Li, L. Zhang, D. Zhai, Y. Li, S. Zhang, M. Li, L. Kang, J. Chen, and P. Wu, "Satellite laser ranging using superconducting nanowire single-photon detectors at 1064 nm wavelength," Opt. Lett. **41**(16), 3848–3851 (2016).
40. H. Li, S. Chen, L. You, W. Meng, Z. Wu, Z. Zhang, K. Tang, L. Zhang, W. Zhang, and X. Yang, "Superconducting nanowire single photon detector at 532 nm and demonstration in satellite laser ranging," Opt. Express **24**(4), 3535–3542 (2016).
41. B. Zhang, Y.-Q. Guan, L. Xia, D. Dong, Q. Chen, C. Xu, C. Wu, H. Huang, L. Zhang, L. Kang, J. Chen, and P. Wu, "An all-day lidar for detecting soft targets over 100 km based on superconducting nanowire single-photon detectors," Supercond. Sci. Technol. **34**(3), 034005 (2021).
42. X.-T. Fang, P. Zeng, H. Liu, M. Zou, W. Wu, Y.-L. Tang, Y.-J. Sheng, Y. Xiang, W. Zhang, and H. Li, "Implementation of quantum key distribution surpassing the linear rate-transmittance bound," Nat. Photonics **14**(7), 422–425 (2020).
43. D. Salvoni, A. Boselli, A. Sannino, L. Parlato, M. Ejrnaes, Z. Chengjun, L. You, X. Wang, S. Amoruso, and G. P. Pepe, "Demonstration of atmospheric lidar measurement in the infrared wavelength domain with a superconducting nanowire single photon detector," Chemical Engineering Transactions **84**, 175–180 (2021).
44. J. Qiu, H. Xia, M. Shangguan, X. Dou, M. Li, C. Wang, X. Shang, S. Lin, and J. Liu, "Micro-pulse polarization lidar at 1.5 μm using a single superconducting nanowire single-photon detector," Opt. Lett. **42**(21), 4454–4457 (2017).
45. S. Yu, Z. Zhang, H. Xia, X. Dou, T. Wu, Y. Hu, M. Li, M. Shangguan, T. Wei, and L. Zhao, "Photon-counting distributed free-space spectroscopy," Light: Sci. Appl. **10**(1), 212 (2021).
46. C. Lv, H. Zhou, H. Li, L. You, X. Liu, Y. Wang, W. Zhang, S. Chen, Z. Wang, and X. Xie, "Large active area superconducting single-nanowire photon detector with a 100 μm diameter," Supercond. Sci. Technol. **30**(11), 115018 (2017).
47. A. J. Kerman, E. A. Dauler, W. E. Keicher, J. K. Yang, K. K. Berggren, G. Gol'Tsman, and B. Voronov, "Kinetic-inductance-limited reset time of superconducting nanowire photon counters," Appl. Phys. Lett. **88**(11), 111116 (2006).
48. J. Allmaras, A. Beyer, R. Briggs, F. Marsili, M. Shaw, G. Resta, J. Stern, V. Verma, R. Mirin, and S. Nam, "Large-area 64-pixel array of WSi superconducting nanowire single photon detectors," in *CLEO: Applications and Technology*, (Optica Publishing Group, 2017), JTh3E. 7.
49. C. Zhang, W. Zhang, J. Huang, L. You, H. Li, C. lv, T. Sugihara, M. Watanabe, H. Zhou, and Z. Wang, "NbN superconducting nanowire single-photon detector with an active area of 300 μm-in-diameter," AIP Adv. **9**(7), 075214 (2019).
50. B. Kaifler, C. Geach, H. C. Büdenbender, A. Mezger, and M. Rapp, "Measurements of metastable helium in Earth's atmosphere by resonance lidar," Nat. Commun. **13**(1), 6042–6047 (2022).
51. V. A. Kovalev and W. E. Eichinger, *Elastic lidar: theory, practice, and analysis methods* (John Wiley & Sons, 2004).
52. M.-H. Kim, A. H. Omar, J. L. Tackett, M. A. Vaughan, D. M. Winker, C. R. Trepte, Y. Hu, Z. Liu, L. R. Poole, and M. C. Pitts, "The CALIPSO version 4 automated aerosol classification and lidar ratio selection algorithm," Atmos. Meas. Tech. **11**(11), 6107–6135 (2018).
53. J. A. Reagan, M. P. McCormick, and J. D. Spinhirne, "Lidar sensing of aerosols and clouds in the troposphere and stratosphere," Proc. IEEE **77**(3), 433–448 (1989).
54. A. A. Kokhanovsky, *Aerosol optics: light absorption and scattering by particles in the atmosphere* (Springer Science & Business Media, 2008).
55. K. F. Palmer and D. Williams, "Optical constants of sulfuric acid; application to the clouds of Venus?" Appl. Opt. **14**(1), 208–219 (1975).
56. T. Fujii and T. Fukuchi, *Laser remote sensing* (CRC press, 2005).
57. F. Rocadenbosch, S. Frasier, D. Kumar, D. L. Vega, E. Gregorio, and M. Sicard, "Backscatter error bounds for the elastic lidar two-component inversion algorithm," IEEE Trans. Geosci. Remote Sensing **50**(11), 4791–4803 (2012).
58. V. Gorshelev, A. Serdyuchenko, M. Weber, W. Chehade, and J. Burrows, "High spectral resolution ozone absorption cross-sections–Part 1: Measurements, data analysis and comparison with previous measurements around 293 K," Atmos. Meas. Tech. **7**(2), 609–624 (2014).
59. J. Zhang, X. Wu, J. Bian, X. Xia, Z. Bai, Y. Liu, Z. Cai, J. Huo, and D. Lyu, "Aerosol variations in the upper troposphere and lower stratosphere over the Tibetan Plateau," Environ. Res. Lett. **15**(9), 094068 (2020).